Desalination 615 (2025) 119260

Contents lists available at ScienceDirect

Desalination

journal homepage: www.elsevier.com/locate/desal

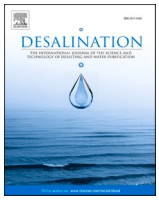

Synergistic modification of spinel $LiMn_2O_4$ with MgO doping and coating for mitigating the Jahn-Teller effect and enhancing lithium extraction from brine

Wenjie Fan [a], Luxiang Ma [a,b,*], Wencheng Pan [a], Xin Zeng [a], Zhixiang Li [a], Hongli Su [c], Peng Zhang [d], Yan Zhao [a]

[a] College of Materials and Chemistry & Chemical Engineering, Cheng Du University of Technology, Cheng Du 610059, PR China
[b] Salt Lake Chemical Engineering Research Complex, Qinghai University, PR China
[c] Resource & Recycling, Department of Engineering Structures, Faculty of Civil Engineering and Geosciences, Delft University of Technology, Delft 2628, CN, the Netherlands
[d] Binzhou Yellow River Affairs Bureau, Boxing Yellow River Affairs Bureau, PR China

HIGHLIGHTS

- Gradient doping and MgO coating mitigate Jahn-Teller distortion and Mn dissolution in $LiMn_2O_4$ during cycling.
- Retained 81.8 % capacity after 20 cycles in the West Taijinar old brine.
- $LiMn_2O_4$@MgO exhibited only 0.34 % Mn dissolution after 20 cycles.
- Effectively reducing the Mg^{2+}/Li^+ ratio in low-grade brine.

ARTICLE INFO

Keywords:
Electrochemical lithium extraction
Spinel $LiMn_2O_4$
Jahn-Teller effect
Gradient doping-coating synergistic modification
DFT calculations

ABSTRACT

$LiMn_2O_4$ (LMO) has emerged as a promising electrode material for the electrochemical extraction of lithium from salt lakes due to its excellent lithium-ion selectivity and structural stability. However, the cyclic use of LMO in Salt Lake brines is often hindered by manganese dissolution and crystal structure collapse, primarily caused by the Jahn-Teller effect. These issues significantly reduce the cycling stability and lithium extraction efficiency of LMO, limiting its practical application. To address this challenge, we developed a molten salt-assisted gradient doping-coating synergistic modification technique aimed at effectively suppressing the Jahn-Teller effect. This approach facilitates the formation of chemically bonded MgO nanolayers on the LMO surface and incorporates Mg^{2+} into the bulk structure, thereby significantly enhancing the material's structural stability. Through a combination of density functional theory (DFT) calculations and experimental validation, the modified composite electrode exhibited superior kinetic performance, high capacity, and remarkable cycling stability. In simulated brine, it maintained a lithium adsorption capacity of 26.21 $mg{\cdot}g^{-1}$ after 20 consecutive extraction cycles. Furthermore, in the West Taijinar old brine with a high Mg^{2+}/Li^+ ratio of 65.6, the modified electrode demonstrated a capacity retention rate of 81.8 %, approximately 34 % higher than pristine LMO, and reduced the Mg^{2+}/Li^+ ratio from 65.6 to 0.24. Furthermore, the modified electrode exhibited a manganese dissolution rate of only 0.34 %. These findings indicate that the proposed modification strategy significantly improves the cycling stability and lithium extraction performance of LMO, offering a viable pathway for its large-scale application in Salt Lake environments.

1. Introduction

Lithium is a strategic critical material that plays an essential role in power battery manufacturing clean energy transition, and the development of national defense technologies [1]. According to International Energy Agency (IEA) statistics, global lithium demand surged from

* Corresponding authors.
E-mail address: maluxiang@cdut.edu.cn (L. Ma).

https://doi.org/10.1016/j.desal.2025.119260
Received 3 July 2025; Received in revised form 25 July 2025; Accepted 29 July 2025
Available online 29 July 2025

32,000 metric tons in 2015 to 134,000 metric tons in 2022, with projections exceeding 1.5 million metric tons by 2030 [2]. Current industrial lithium extraction methods primarily include ore-based and brine-based systems [3,4]. However, ore-based extraction, which is energy-intensive and environmentally challenging, is increasingly being replaced by brine extraction due to its relatively lower environmental impact [5]. Brine extraction techniques encompass seawater, groundwater, oilfield water, and salt-lake brines [6–8]; the first three face limitations including ultra-low Li^+ concentration (<0.2 ppm), severe Mg^{2+}/Ca^{2+} interference, and uneven geographical distribution [2]. Therefore, the exploration of lithium from salt-lake brine and seawater is a good alternative to address the issue of lithium shortage the lithium extraction technologies mainly include the adsorption , precipitation, solvent extraction, membrane separation, and electrochemical methods [9–12]. In particular, the electrochemical intercalation method, as an emerging electrochemical lithium extraction technology, has attracted significant attention due to its advantages of high adsorption capacity, high selectivity for lithium ions, low energy consumption, ease of regeneration, and environmental friendliness [13].

Electrode materials represent a critical factor determining the lithium extraction performance in the electrochemical deintercalation process. To date, lithium electrode materials that have been employed for selective lithium extraction via the electrochemical deintercalation method primarily include two categories: lithium iron phosphate ($LiFePO_4$) and spinel-type lithium manganese oxide (LMO). Among these, $LiFePO_4$ exhibits extremely low electronic conductivity ($<10^{-9}$ S/cm) due to its inherent structural characteristics — specifically, the discontinuous conductive network formed by FeO_6 octahedra and PO_4 tetrahedra — while the geometric constraints imposed by PO_4 tetrahedra on Li^+ diffusion pathways markedly reduce lithium-ion mobility ($\sim 10^{-14}$ cm^2/s) [14]. These intrinsic structural characteristics induce an inherent “trade-off” effect between lithium extraction capacity and selectivity, constituting a fundamental bottleneck at the material level that restricts lithium extraction performance. In contrast, LMO has emerged as a superior electrode candidate for Li^+ extraction due to its higher electrochemical activity, greater specific capacity, and enhanced selectivity [15]. The spinel-structured LMO possesses distinctive Li^+ occupation sites and three-dimensional Li^+ diffusion channels [16], which significantly facilitate the transport and storage of Li^+ [15].

However, extended cycling of this material induces structural distortion due to the Jahn-Teller effect. This arises from elongational distortion of the Mn^{3+} local octahedra. Although the long-range cubic symmetry is preserved due to the disordered distribution of Mn^{3+}/Mn^{4+}, the dynamic fluctuation of these distortions leads to lattice instability, phase transitions, and ultimately, structural collapse of the crystal, resulting in the blockage of Li^+ transport channels [18].Additionally, electrolyte-induced surface reconstruction promotes the formation of a Mn_3O_4 phase, which facilitates the Mn^{3+} disproportionation reaction ($2Mn^{3+} \rightarrow Mn^{2+} + Mn^{4+}$) [19]. The subsequent dissolution of Mn^{2+} exacerbates manganese dissolution, further degrading the electrode’s performance. Therefore, addressing the structural distortion of $LiMn_2O_4$ and mitigating manganese dissolution represent one of the primary challenges currently facing this material.

Mn dissolution and interfacial side reactions originate primarily from the surface instability of electrode materials, thus rendering surface modification strategies effective in alleviating these issues. For example, constructing a ZnO modification layer on the material surface not only enhances the electrode’s hydrophobicity and reduces electrolyte corrosion, but also selectively suppresses Mn dissolution and promotes lithium-ion transport [20]. The $AlPO_4$ interface modification can simultaneously enhance the lithium-ion migration rate and mitigate side reactions, thereby significantly improving the cycling stability [21]. Furthermore, targeting the structural distortion induced by the Jahn-Teller effect, bulk doping (e.g., Cr^{3+}, Mg^{2+}) and interface engineering (e.g., MgO coating) have been experimentally validated to effectively stabilize the spinel structure [22]. However, the current strategies (single-component doping or modification) often only address specific issues: while doping can suppress Jahn-Teller distortion, it fails to prevent interfacial Mn dissolution; although surface coating protects the interface, it struggles to regulate the bulk structural stability. Such constraints expose the material to a risk of synergistic failure during prolonged cycling [23]. Therefore, developing a multi-effect synergistic strategy integrating surface/bulk modifications to simultaneously suppress the Jahn-Teller effect, Mn dissolution, and interfacial side reactions is of great significance for advancing the commercialization of high-stability Mn-based electrodes.

In this work, we propose a molten-salt-assisted gradient doping-coating synergistic modification approach, which achieves both the construction of chemically bonded MgO nanolayers with tunable thickness and gradient bulk doping of Mg^{2+} through controlled addition of MgO.(Fig. 1). This strategy not only suppresses Jahn-Teller-induced lattice distortion but also mitigates Mn dissolution and interfacial side reactions, while the chemical bonding simultaneously enhances Li-ion mobility. In the West Taijinar old brine with an Mg/Li ratio as high as 65.6, the modified $LiMn_2O_4$@MgO (LMO@MgO) electrode maintained 82 % lithium extraction efficiency after 20 cycles, showing a nearly 30 % improvement compared to the pristine sample. First-principles DFT calculations further elucidated the evolution of the band structure and the reduction mechanism of lithium diffusion energy barriers in the composite electrode system. This study provides an innovative solution for efficient exploitation of high-Mg/Li ratio Salt Lake resources.

2. Experimental section

2.1. Preparation of powder materials and electrodes

Lithium manganese oxide (LMO) was synthesized via a solid-state reaction [24]. Mn_2O_3 and $LiOH{\cdot}H_2O$ were mixed at a molar ratio of 1:1.05 (with 5 mol% excess $LiOH{\cdot}H_2O$ to compensate for lithium volatilization at high temperatures) [25]. The MgO doping level in LMO was controlled by varying the molar ratio of MgO to Mn_2O_3 to 0.01:1, 0.05:1, and 0.1:1, yielding four powder materials: pristine LMO, LMO-Mg1, LMO-Mg5, and LMO-Mg10. The ground mixture was preheated at 500 °C for 5 h in air, then heated to 750 °C at a heating rate of 5 °C/min and maintained at this temperature for 20 h, followed by natural cooling to room temperature to obtain the desired sample. The resulting powders were then mixed with conductive additives and binders and pressed into 2 cm × 2 cm LMO@MgO electrode sheets.

2.2. Electrochemical performance testing

The electrochemical performance of the electrode materials and devices was characterized using an Autolab PGSTATs electrochemical workstation (Switzerland). A three-electrode system was employed in 0.1 M LiCl aqueous solution, with $LiMn_2O_4$ as the working electrode, platinum (Pt) as the counter electrode, and K/KCl as the reference electrode. The measurements included: Cyclic Voltammetry (CV) with a voltage window of −0.99 to 0.99 V and a scan rate of 0.2 mV/electrochemical Impedance Spectroscopy (EIS) performed over a frequency range of 0.001 Hz to 100 kHz, with multiple scans to ensure reproducibility. Additionally, long-term cycling and rate capability tests were conducted at a current density of 0.783 μA/mm^2.

2.3. Study of the effect of impurity on Li^+ selectivity in real brines

The research focused on utilizing the West Taijinar old brine as the subject of investigation. Specifically, a 1:1 dilution of the West Taijinar old brine was introduced into the anode chamber, while KCl solution was added to the cathode chamber. The anode was constructed using an LMO@MgO electrode, and Mn_2O_4 served as the cathode material. A voltage of 0.8 V was applied across the system, and the concentrations of Li^+, Na^+, Mg^{2+}, and K^+ ions in the solution were subsequently analyzed

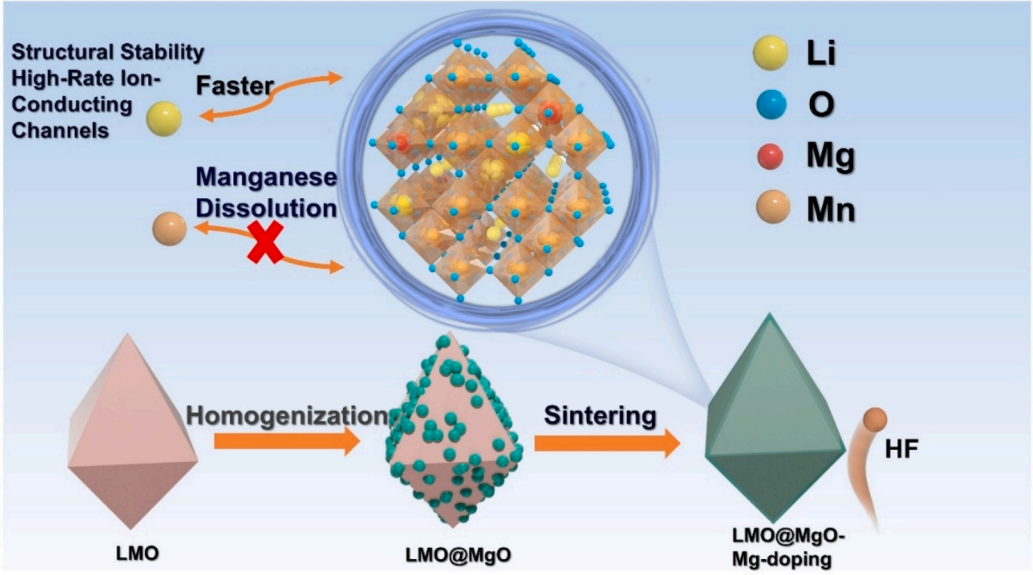

Fig. 1. LMO@MgO preparation diagram.

using inductively coupled plasma (ICP) spectroscopy.

2.4. Characterization

All chemicals used were of analytical grade. Crystal structures were analyzed by X-ray diffraction (XRD, Bruker D8 ADVANCE, Cu Kα radiation, 40 kV, 40 mA) with a 2θ scanning range of 10°–80°, a scan rate of 5° min^{-1}, and a step size of 0.02°. Morphology and crystallinity were examined using field emission scanning electron microscopy with energy-dispersive X-ray spectroscopy (FE-SEM/EDS, FEI Quantum 650, USA) and high-angle annular dark-field scanning transmission electron microscopy (HAADF-STEM, JEOL JEM-2100F, Japan). Elemental distribution mapping was performed via EDS (ZEISS Gemini SEM 300). Chemical states were probed by X-ray photoelectron spectroscopy (XPS, Shimadzu/Kratos AXIS Ultra DLD).

2.5. DFT calculation

In this study, electronic structure calculations were performed using the Projector Augmented Wave (PAW) method within Density Functional Theory (DFT), as implemented in the Vienna Ab initio Simulation Package (VASP) [26,27]. The Perdew-Burke-Ernzerhof (PBE) exchange-correlation functional was employed for energy minimization [28], with a plane-wave basis set energy cutoff of 500 eV applied on a singular k-point grid. Additionally, the GGA + U approach [29] was adopted to address the self-interaction error inherent in standard DFT and to account for strong 3d electron correlations in transition metals. This method utilized an effective U value (Ueff = U − J, with J = 1 eV), where a U value of 3.5 eV was applied to Mn [30]. Partial occupancies of the Kohn-Sham orbitals were treated using the Gaussian smearing method with a width of 0.05 eV. Self-consistency in electronic energy was achieved when the energy variation fell below 2 × 10ˆ−5 eV, while geometric optimizations were considered complete when energy reductions were less than 0.05 eV. The equilibrium lattice constants were first optimized using a 3 × 1 × 1 Monkhorst-Pack k-point mesh, followed by detailed electronic structure calculations performed on a 1 × 2 × 1 grid.

3. Results and discussion

3.1. Morphological structure analysis of composite materials

XRD offers a potent tool for elucidating the crystallographic structure of electrode materials. As depicted in Fig. 2a, the LMO sample exhibits a characteristic spinel structure belonging to the Fd3m space group. Notably, the introduction of Mg^{2+} via doping does not induce any discernible alteration in the fundamental structural attributes of LMO. Specifically, the diffraction peaks observed at 36°, 44°, and 64° can be unambiguously assigned to the (311), (400), and (440) crystallographic planes, respectively. These observations are in excellent concurrence with the reference pattern documented in PDF#35–0782. Both the synthesized LMO and LMO@MgO exhibit sharp and well-defined Bragg diffraction peaks, which closely match the standard XRD reference pattern for LMO [31]. Simultaneously, the respective electrode materials were dissolved, and their ionic contents were measured (**Table S1**). The results are consistent with the relevant elemental stoichiometric ratios, confirming the correctness of the chemical formulae.

As can be observed in the locally magnified XRD patterns shown in Fig. 2b, the (400) diffraction peaks for LMO, LMO-Mg1, LMO-Mg5, and LMO-Mg10 progressively shift to higher angles with increasing MgO content. Based on Bragg's law ($2d\,sin\theta = n\lambda$), the shift occurs because the smaller-radius Mg^{2+} substitute for the larger-radius Mn^{3+} ions. Calculations further reveal a gradual reduction in the lattice parameter upon MgO addition(**Fig. S1,Table S2**).These results indicate that Mg^{2+} ions have been successfully doped into the LMO lattice [32].

The surface morphology of the samples was characterized using FE-SEM. As shown in Fig. 2c-d and **S2**,all samples (LMO, LMO-Mg1, LMO-Mg5, LMO-Mg10) exhibited incomplete octahedral geometries characteristic of spinel structures, with particle sizes ranging from 100 nm to 1 μm [33]. The EDS mapping (Fig. 2e) corroborated homogeneous magnesium distribution across the LMO matrix [34].

HAADF-STEM provided direct visualization of MgO deposition on LMO substrates. Specifically, lattice fringe analysis at LMO@MgO intergranular sites revealed distinct d-spacings of 0.13 nm (Fig. 2g), matching standard MgO (220) planes as confirmed by XRD. Within pristine LMO regions, (111) plane spacing measured 0.47 nm (Fig. 2f), consistent with XRD findings. Remarkably, this interplanar distance contracted to 0.41 nm in LMO@MgO, attributed to substitutional doping of smaller Mg^{2+} into larger Mn^{3+} sites within the spinel lattice. Further structural validation was obtained through HAADF-STEM diffraction patterning (Fig. 2h), which displayed well-defined spots corresponding to LMO's (111) and (133) crystallographic planes This preservation of long-range order confirms that MgO integration maintains the integrity of the original spinel structure [35].

The XPS was conducted to elucidate the electronic structure

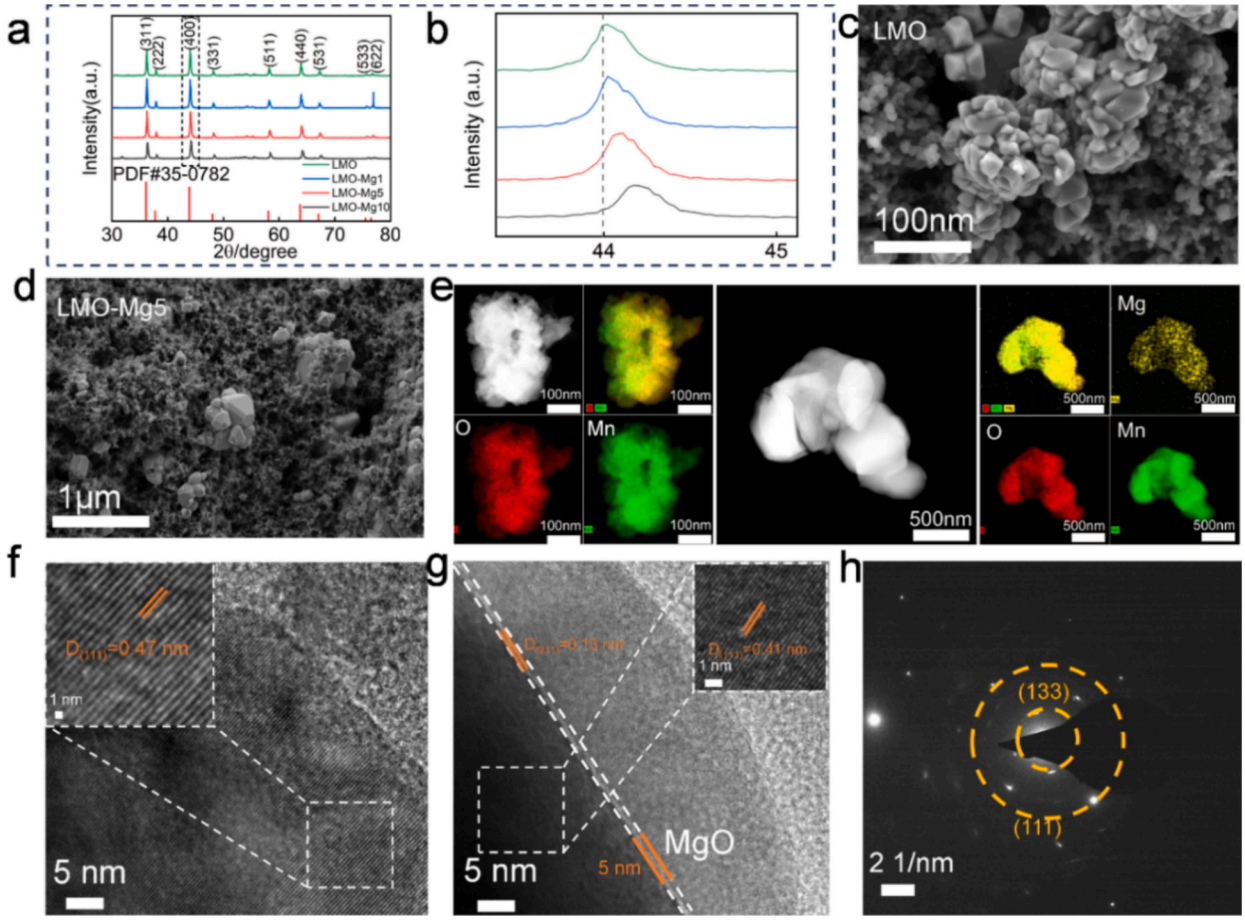

Fig. 2. Structural and morphological characterizations: (a-b) XRD patterns with corresponding local magnifications for the synthesized samples. (c) and (d) exhibit FE-SEM images of LMO and LMO-Mg5, respectively. (e) presents EDS mappings for both LMO and LMO@MgO. HAADF-STEM micrographs of LMO and LMO@MgO are shown in (f) and (g), while (h) illustrates the HAADF-STEM diffraction pattern of LMO@MgO.

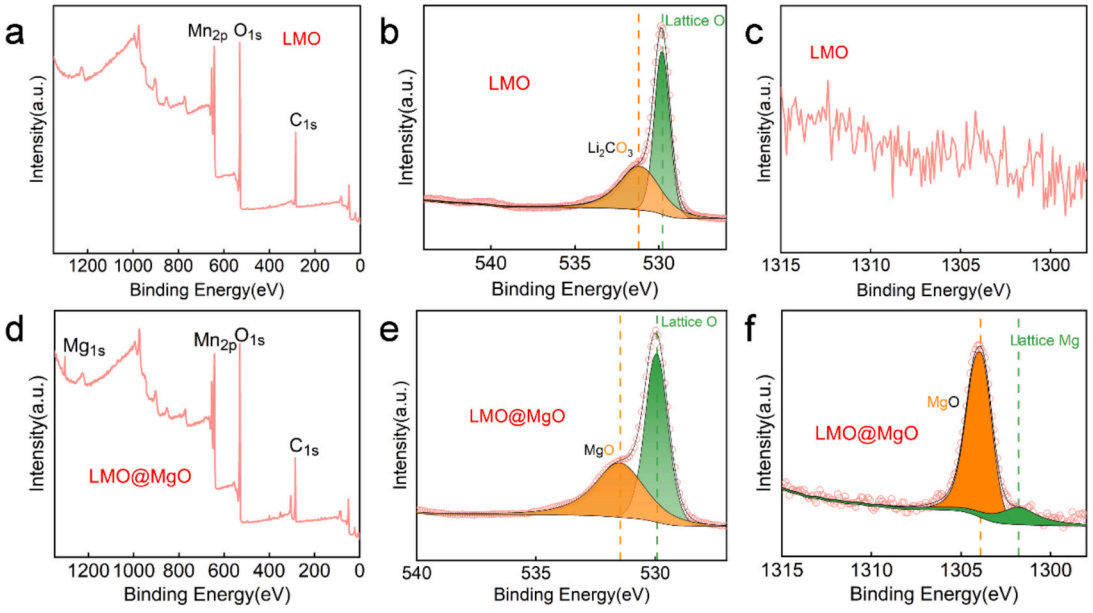

Fig. 3. Surface composition and interface characterization of synthesized samples: (a, d) Wide-scan XPS spectra of pristine LMO and LMO@MgO, respectively; (b) O 1 s core-level spectrum of LMO; (c) Mg 1 s core-level spectrum of LMO (control); (e) O 1 s core-level spectrum of LMO@MgO; (f) Mg 1 s core-level spectrum of LMO@MgO.

evolution, with representative spectra for LMO@MgO and pristine LMO presented in Fig. 3. The survey spectrum of LMO@MgO (Fig. 3a) revealed an additional Mg 1 s peak at 1303.9 eV (Fig. 3d), closely matching the binding energy of crystalline MgO [36]. This characteristic peak unambiguously verifies the successful deposition of magnesium-containing species on the LMO surface. Notably, the O 1 s spectral deconvolution (Fig. 3b,e) showed a significant enhancement of the component centered at 531.5 eV for LMO@MgO, which aligns with the oxygen binding energy in MgO (531.3 eV) [37]. This observation starkly contrasts with pristine LMO, where the dominant O 1 s feature at 531.2 eV corresponds to carbonate impurities (Li_2CO_3) [38,39]. The systematic shift in oxygen signatures provides compelling evidence for preferential surface modification rather than bulk alteration. Such spectral variations collectively confirm the formation of a conformal MgO coating layer on LMO particles, as corroborated by both cationic and anionic species analysis.

3.2. Electrochemical performance analysis

To systematically evaluate the adsorption selectivity of LMO and LMO@MgO toward Li^+, Na^+, K^+, and Mg^{2+} in saline environments, The CV analyses were performed in 0.1 M LiCl, NaCl, KCl, and $MgCl_2$ electrolytes (Fig. 4a-h). Notably, both pristine LMO and Mg-doped samples exhibited a distinctive oxidation peak near 0.74 V in LiCl solution (Fig. 4a,e), characteristic of Li^+ deintercalation [40]. Remarkably, LMO-Mg5 demonstrated a 43.5 % enhancement in peak current density (3.53 mA vs. 2.46 mA for LMO at identical scan rates), which was attributed to facilitated Li^+ transport kinetics resulting from reduced diffusion barriers after Mg^{2+} doping [21]. This performance advantage was further corroborated by comparative analysis, where LMO-Mg5 outperformed LMO-Mg1 (2.70 mA) and LMO-Mg10 (2.80 mA) in peak current magnitude (Fig. 4i, **S3**). In NaCl and KCl electrolytes (Fig. 4b,c,f,g), LMO-Mg5 displayed a single dominant oxidation peak corresponding to initial Li^+ extraction, suggesting enhanced ion selectivity compared to unmodified LMO. Even in $MgCl_2$ solution, where Mg^{2+} (0.72 Å) competes with Li^+ (0.76 Å) for surface adsorption [40], both LMO and LMO-Mg5 exhibited detectable Mg^{2+} extraction signals (Fig. 4d,h). Crucially, the CV profiles of LMO-Mg5 consistently featured sharper, more symmetric redox peaks relative to pristine LMO, indicative of improved reaction reversibility and kinetics. This phenomenon highlights the synergistic effects of Mg^{2+} doping and MgO surface coating in promoting uniform electrochemical processes [41].

Further kinetic and stability evaluations of LMO@MgO included EIS, rate capability, and long-cycle testing. EIS results (Fig. 5a, **Table S3**) indicate that the charge transfer resistances of LMO-Mg1 (15.4 Ω) and LMO-Mg5 (14.4 Ω), which are doped with appropriate amounts of Mg^{2+}, are significantly lower than that of pristine LMO (17.1 Ω). This can also be attributed to the incorporation of Mg^{2+}, which lowers the energy barrier for Li^+ migration, thereby fundamentally reducing the intrinsic impedance of LMO@MgO. (Fig. 7b) [42]However, the resistance of LMO-Mg10, which is excessively coated with MgO, increases substantially to 22.1 Ω, primarily due to the thick coating layer hindering Li^+ migration, further inhibiting Li^+ diffusion kinetics [43]. LMO-Mg5 achieved equilibrium significantly faster, reaching a lithium extraction capacity of 22.65 $mg{\cdot}g^{-1}$ within 60 min (Fig. 5b). In contrast, the LMO electrode required 80 min to reach the corresponding capacity of 22.65 $mg{\cdot}g^{-1}$. This performance enhancement originates from the reduction of the Li^+ diffusion energy barrier via Mg^{2+} doping in LMO, thereby

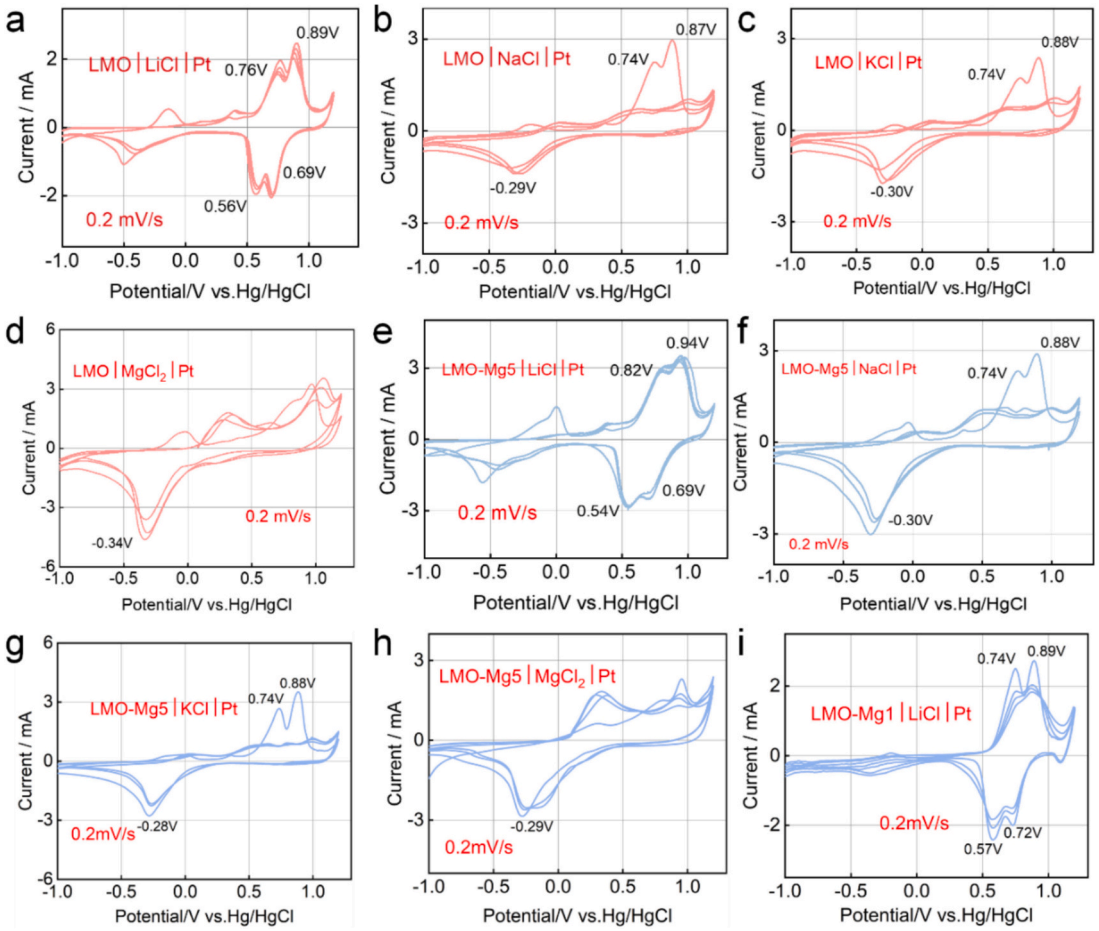

Fig. 4. CV curves of the electrode: Electrodes(a-h) CV curves of the materials in LiCl, NaCl, KCl, and $MgCl_2$ solutions. (i) CV image of LMO-Mg1 in LiCl.

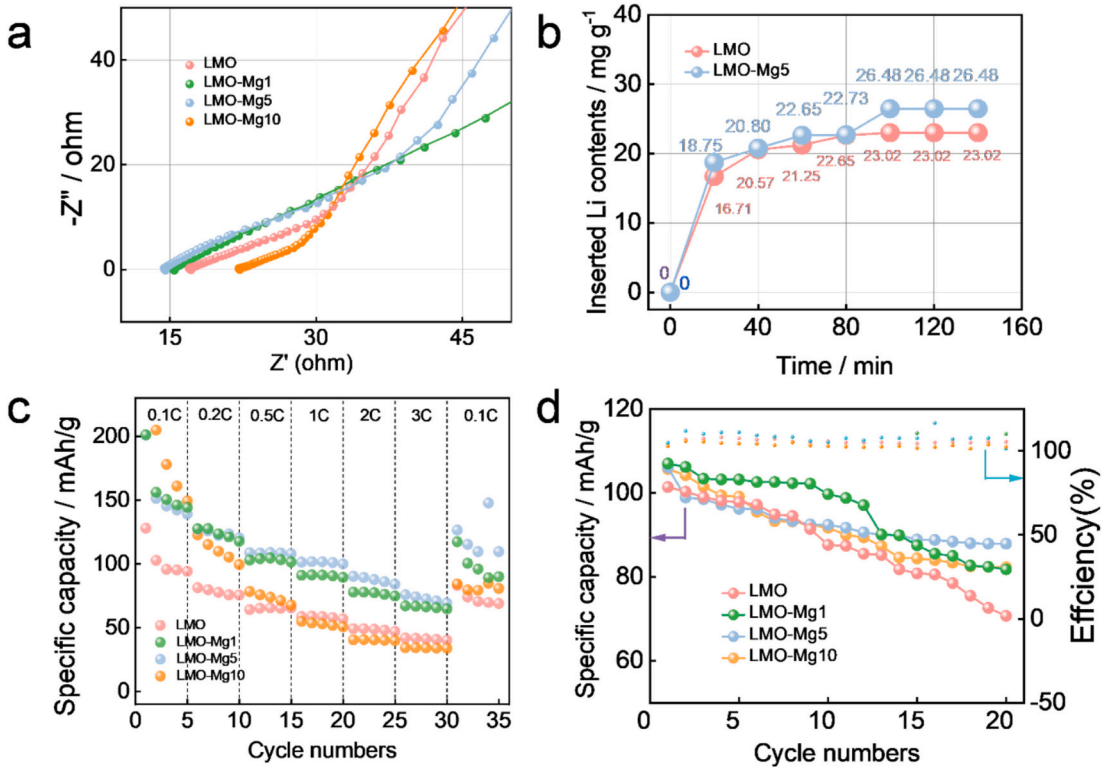

Fig. 5. Electrochemical performance of the electrodes: (a) EIS spectra of the materials. (b) Correlation between Li^+ extraction capacity and time. (c)Discharge capacity of materials with different rates. (d)Long-term cycling performance of the materials.

lowering its ohmic resistance and resulting in remarkable kinetic performance(Fig. 7) [44]. Rate capability tests for each electrode material are shown in **Fig. 5**c. Although the discharge capacities of all materials decrease with increasing rate, the performance of LMO-Mg5 consistently surpasses that of LMO at all rates and most effectively recovers its initial capacity after rate changes, highlighting its electrochemical reversibility and structural integrity in aqueous environments. This suggests that the addition of MgO endows the LMO electrode with superior resistance to high current densities and enhanced kinetic performance. **Fig. 5**d shows that after 20 cycles, LMO-Mg5 exhibits superior stability with a capacity retention rate of 82.8 %, while the capacity of LMO decreases to 101.3 mAh/g with a retention rate of only 69.7 %. This indicates that the doping and coating of Mg^{2+} and MgO successfully alleviate lattice distortion caused by the Jahn-Teller effect, protect LMO from brine corrosion significantly enhancing the cycling stability of LMO and ensuring long-term Li^+ extraction stability [45].

3.3. *Lithium extraction performance analysis of composite electrodes*

Fig. 6 compares the lithium extraction performance of electrodes in simulated and real brine. To evaluate the feasibility of the LMO@MgO electrode, the optimized LMO-Mg5 composite material was assessed in an artificial brine environment (Mg^{2+}/Li^+ = 28.6, **Table S4**,28 °C) designed to simulate the ionic complexity of natural brines. As shown in **Fig. 6**a and b, it achieved a stable extraction capacity exceeding 26.21 $mg{\cdot}g^{-1}$ with a lithium extraction efficiency of 67.7 % over 20 cycles. Notably, the Mg^{2+}/Li^+ ratio decreased to 0.24 post-cycling (**Fig. 6**c), confirming its excellent magnesium-lithium separation capability. This enhancement in Li^+ insertion selectivity primarily arises from the Mg^{2+} incorporation, which modulates the lattice parameters, expands the dimensions of the 3D Li^+ diffusion pathways (8a → 16c sites), and concurrently lowers the Li^+ migration energy barrier [46]. In real brine (Mg^{2+}/Li^+ = 65.6, **Table S5**, 29 °C), the LMO-Mg5 electrode maintained a lithium selectivity of 63.3 % and a stable capacity of 24.5 $mg{\cdot}g^{-1}$ after 20 cycles—a 34 % improvement over pristine LMO (**Fig. 6**d–f). The Mg^{2+}/Li^+ ratio similarly reduced to 0.24, demonstrating its adaptability to high-magnesium environments. The observed performance discrepancy between simulated and authentic brine samples can be attributed to the higher ionic strength from impurities and the complex microbial environment in authentic brine, which collectively reduce Li^+ extraction capacity. Nevertheless, LMO@MgO demonstrates an exceptional Mg^{2+}/Li^+ separation selectivity ratio even in authentic brine, underscoring its significant industrial relevance.

Crucially, while excessive surface coating without bulk doping (e.g., LMO-Mg10) mitigates surface corrosion, it fails to suppress the lattice distortion induced by the Mn^{3+}-driven Jahn-Teller effect. Moreover, the presence of an over-thick coating layer significantly impedes Li^+ transport [30].This leads to rapid capacity decay in later cycles, as evidenced by the sharp drop in lithium extraction efficiency from 62.5 % to 36.7 % between cycles 15–20 in real brine (**Fig. 6**e). Conversely, minimal doping without surface protection (e.g., LMO-Mg1) stabilizes the bulk phase but allows surface erosion, resulting in an initial capacity decline of ~10 % within five cycles (from 29.71 to 23.15 $mg{\cdot}g^{-1}$, **Fig. 6**a–b). These findings highlight that synergistic bulk doping and surface coating are essential for balancing structural stability, surface protection, and long-term cyclability in LMO@MgO electrodes.

Furthermore, the Mn^{2+} content in the recovered solution and the manganese dissolution rate were measured and calculated during the cycling process. As shown in **Fig. 6**i, the Mn^{2+} content and manganese dissolution rate for both LMO and LMO-Mg5 increase progressively with the number of cycles. Remarkably, the manganese dissolution rate of LMO-Mg5 is significantly lower than that of pristine LMO. After 20 cycles, the dissolution rate of pristine LMO reaches a substantial 29 %, whereas that of LMO-Mg5 is only 0.34 %.

To elucidate the origin of this phenomenon, XPS measurements of the Mn 2p spectra were conducted on both pristine LMO and LMO@MgO (**Fig. 6**g-h). The ratio of Mn^{4+} to Mn^{3+} in pristine LMO is 0.88, corresponding to an average Mn oxidation state of approximately

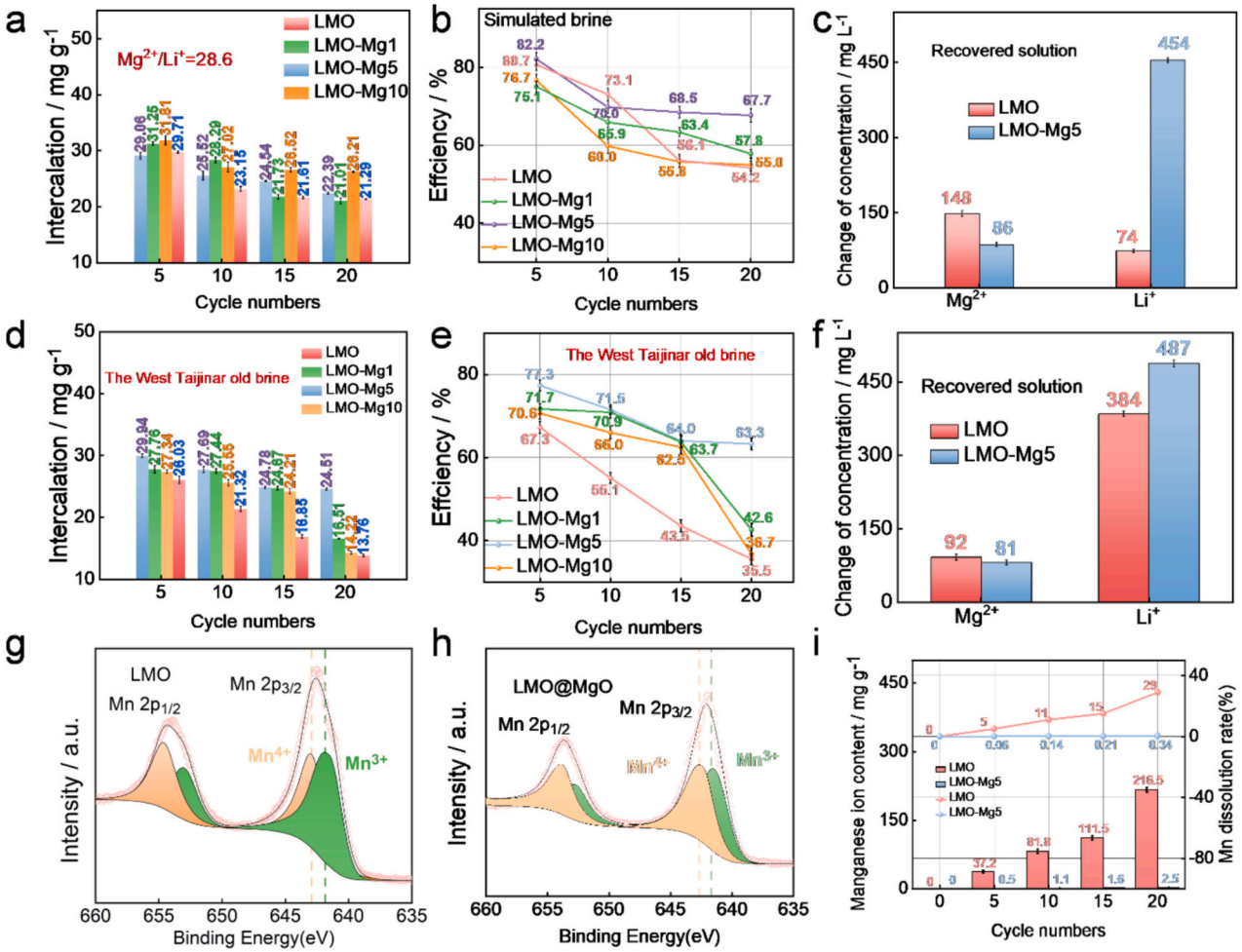

Fig. 6. Electrochemical lithium extraction performance of the electrodes. (a) Li^+ intercalation capacity in simulated brine. (b) Lithium extraction efficiency in actual brine. (c) Li^+ and Mg^{2+} concentrations in solution after electrochemical cycling in simulated brine. (d) Lithium extraction capacity in actual brine. (e) Lithium extraction efficiency in actual brine. (f) Li^+ and Mg^{2+} concentrations in solution after electrochemical cycling in actual brine. (g) Mn 2p XPS spectra of pristine LMO. (h) Mn 2p XPS spectra of LMO@MgO. (i) Manganese ion concentration in the recovered solution and corresponding manganese dissolution rate during cycling.

3.47, which aligns with the average Mn oxidation state of 3.5 in the spinel structure [47]. In contrast, the Mn^{4+} to Mn^{3+} ratio in LMO@MgO increases to 1.23, and the Mn^{3+}/Mn^{4+} redox peaks exhibit a more symmetrical shape. This is attributed to Mg^{2+} doping occupying specific Mn^{3+} sites, resulting in a reduction of Mn^{3+} content and a concomitant increase in Mn^{4+} content due to charge compensation [48]. Consequently, the Jahn-Teller distortion induced by the unfilled d orbitals of Mn^{3+} is suppressed [49], and the propensity for Mn dissolution via Mn^{3+} disproportionation is mitigated [47]. Furthermore, as previously demonstrated, the MgO surface coating on LMO forms a physical barrier. This barrier prevents corrosion of the LMO surface by acidic species present in the electrolyte, while also mitigating manganese dissolution from LMO. [50].

Morphological evolution after cycling (**Fig. S4**) provides conclusive evidence for the synergistic stabilization mechanism: Pristine LMO undergoes catastrophic crystallographic disintegration driven by concurrent Jahn-Teller distortion (Mn^{3+}) and dissolution pathways, meanwhile, LMO-Mg5 maintains high spinel phase fidelity (**Fig. S3**c) and effectively suppresses the tetragonal phase transformation**.** This synergistic modification strategy ensures exceptional structural reversibility and cycling durability, ultimately delivering a technologically viable platform for lithium extraction from high-Mg/Li brine resources.

3.4. Mechanism analysis and DFT calculation

The lithium diffusion mechanisms were elucidated through first-principles nudged elastic band (NEB) calculations, which quantitatively assessed the energy barriers for lithium migration to neighboring vacancy sites. Fig. 7a contrasts the diffusion pathways in pristine LMO and the LMO/Mg composite [30], while Fig. 7b presents the corresponding migration energy profiles. A critical reduction of ~0.20 eV in the diffusion barrier was observed for LMO/Mg compared to pristine LMO, indicating thermodynamically favored lithium desorption in the composite system [51]. This finding correlates strongly with the enhanced kinetic performance observed experimentally.

To interpret the electronic origins of improved performance, density functional theory (DFT) calculations were employed to analyze the band structures of LMO and LMO/Mg. As shown in Fig. 7c-d, pristine LMO exhibits an indirect bandgap of 0.745 eV, whereas Mg^{2+} incorporation induces significant band structure modulation, resulting in overlapping conduction and valence bands with a reduced gap of 0.385 eV [51]. This metallic-like behavior enhances electronic conductivity, accelerating electron transport and facilitating efficient charge transfer during electrochemical cycling. Concurrently, the decreased bandgap mitigates ohmic losses and interfacial charge transfer resistance [52], thereby optimizing Li^+ extraction efficiency. In summary, Mg^{2+} doping in LMO substantially improves kinetic properties by lowering lithium migration barriers and enhancing electronic conductivity. Integrative

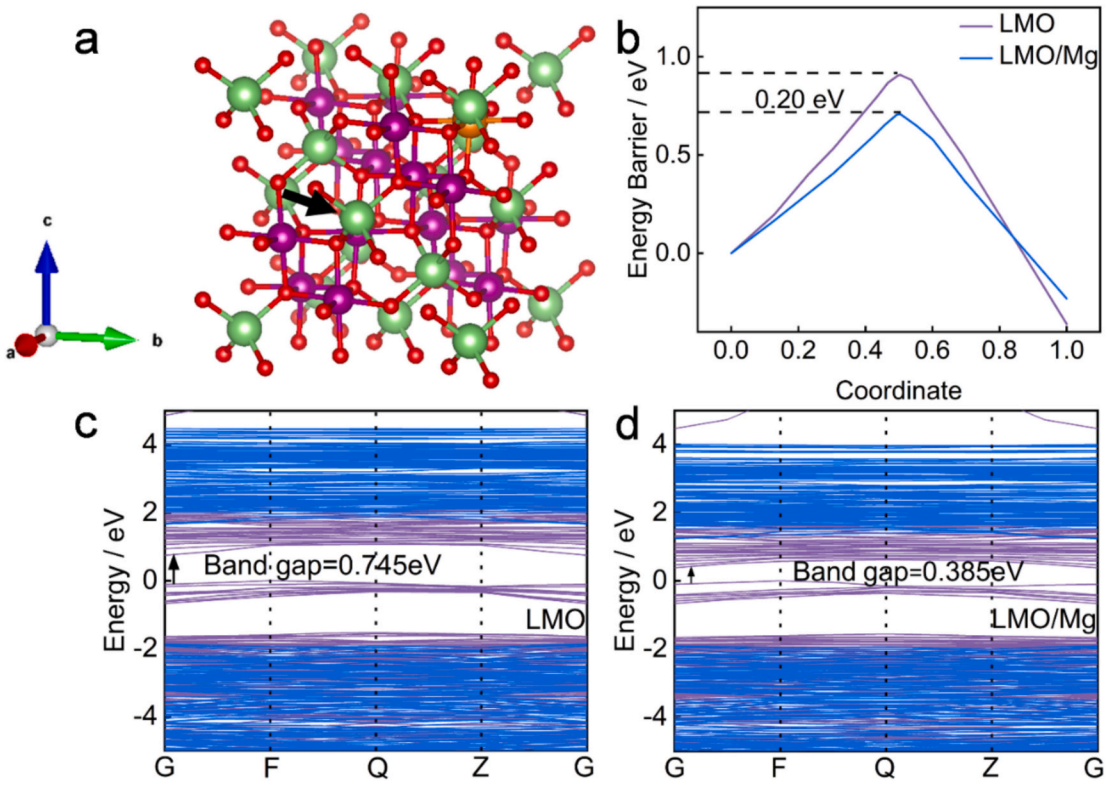

Fig. 7. (a) Migration pathways of Li^+ in LMO and LMO/Mg; (b) The energy barrier magnitudes of LMO and LMO/Mg; (c) and (d) band gaps of LMO and LMO/Mg.

computational-experimental analyses confirm that band structure engineering through cation substitution is a viable strategy to boost charge transfer dynamics in lithium extraction systems.

4. Conclusions

This study established a synergistic Mg^{2+} doping-MgO coating strategy to modulate the valence state of manganese and implement surface engineering in LMO, effectively suppressing the Jahn-Teller effect and mitigating manganese dissolution. Compared to individual coating or doping strategies, this approach simultaneously suppresses Jahn-Teller distortion, manganese dissolution, and interfacial side reactions, while providing a novel pathway toward commercializing high-stability Mn-based electrodes. The optimized LMO@MgO composite electrode demonstrated enhanced electrochemical kinetics and cycling stability, enabling efficient lithium extraction from brine. Notably, in the West Taijinar old brine, the composite electrode demonstrated superior Li^+ intercalation kinetics and an adsorption capacity of 29.94 $mg{\cdot}g^{-1}$ compared to pristine LMO, while maintaining 81.8 % capacity retention after 20 consecutive lithium extraction cycles. Post-cycling analyses confirmed that the surface modification inhibited manganese leaching while maintaining high Li^+ selectivity. This work introduces a viable approach for large-scale electrochemical lithium extraction, advancing the practical application of LMO-based electrodes in resource recovery.

CRediT authorship contribution statement

Wenjie Fan: Writing – review & editing, Investigation, Formal analysis, Data curation, Conceptualization. **Luxiang Ma:** Writing – review & editing, Supervision, Funding acquisition, Formal analysis, Conceptualization. **Wencheng Pan:** Data curation, Conceptualization. **Xin Zeng:** Formal analysis, Data curation. **Zhixiang Li:** Writing – review & editing, Data curation. **Hongli Su:** Writing – review & editing, Data curation. **Peng Zhang:** Writing – review & editing, Data curation. **Yan Zhao:** Formal analysis, Data curation.

Declaration of competing interest

The authors declare no competing financial interest.

Acknowledgments

This research received funding from The Open Project of Salt Lake Chemical Engineering Research Complex, Qinghai University (2025-DXSSKF-12).

Appendix A. Supplementary data

Supplementary data to this article can be found online at https://doi.org/10.1016/j.desal.2025.119260.

Data availability

Data will be made available on request.

References

[1] Y. Ding, N.T.H. Nhung, J. An, H. Chen, L. Liao, C. He, X. Wang, T. Fujita, Manganese-titanium mixed ion sieves for the selective adsorption of lithium ions from an artificial salt lake brine, Materials 16 (2023) 4190.
[2] O. Murphy, M.N. Haji, A review of technologies for direct lithium extraction from low Li^+ concentration aqueous solutions, Front. Chem. Eng. 4 (2022) 1008680.
[3] O. Dolotko, N. Gehrke, T. Malliaridou, R. Sieweck, L. Herrmann, B. Hunzinger, M. Knapp, H. Ehrenberg, Universal and efficient extraction of lithium for lithium-ion battery recycling using mechanochemistry, Communications Chemistry 6 (2023) 49.
[4] C. Dessemond, F. Lajoie-Leroux, G. Soucy, N. Laroche, J.-F. Magnan, Spodumene: the lithium market, resources and processes, Minerals 9 (2019) 334.
[5] M.L. Vera, W.R. Torres, C.I. Galli, A. Chagnes, V. Flexer, Environmental impact of direct lithium extraction from brines, Nature Reviews Earth & Environment 4 (2023) 149–165.

[6] J. Sun, D. Liang, X. Meng, Z. Li, Recent advances in lithium extraction using electrode materials of Li-ion battery from brine/seawater, Processes 10 (2022) 2654.

[7] E.J. Dugamin, A. Richard, M. Cathelineau, M.-C. Boiron, F. Despinois, A. Brisset, Groundwater in sedimentary basins as potential lithium resource: a global prospective study, Sci. Rep. 11 (2021) 21091.

[8] E. Knapik, G. Rotko, M. Marszałek, M. Piotrowski, Comparative study on lithium recovery with ion-selective adsorbents and extractants: results of multi-stage screening test with the use of brine simulated solutions with increasing complexity, Energies 16 (2023) 3149.

[9] H. Su, Z. Li, J. Zhang, W. Liu, Z. Zhu, L. Wang, T. Qi, Combining selective extraction and easy stripping of lithium using a ternary synergistic solvent extraction system through regulation of Fe^{3+} coordination, ACS Sustain. Chem. Eng. 8 (2020) 1971–1979.

[10] H. Bae, Y. Kim, Technologies of lithium recycling from waste lithium ion batteries: a review, Materials advances 2 (2021) 3234–3250.

[11] W. Xu, D. Liu, L. He, Z. Zhao, A comprehensive membrane process for preparing lithium carbonate from high Mg/Li brine, Membranes 10 (2020) 371.

[12] S. Wang, X. Yu, X. Hu, Electrochemical lithium extraction with gas flushing of porous electrodes, Nanomaterials 13 (2023) 1471.

[13] E. Petavratzi, D. Sanchez-Lopez, A. Hughes, J. Stacey, J. Ford, A. Butcher, The impacts of environmental, social and governance (ESG) issues in achieving sustainable lithium supply in the Lithium Triangle, Miner. Econ. 35 (2022) 673–699.

[14] E.V. Antipov, N.R. Khasanova, S.S. Fedotov, Perspectives on Li and transition metal fluoride phosphates as cathode materials for a new generation of Li-ion batteries, IUCrJ 2 (2015) 85–94.

[15] H. Joo, J. Lee, J. Yoon, Short review: timeline of the electrochemical lithium recovery system using the spinel $LiMn_2O_4$ as a positive electrode, Energies 13 (2020) 6235.

[16] Z.-H. Wu, J.-Y. Shih, Y.-J.J. Li, Y.-D. Tsai, T.-F. Hung, C. Karuppiah, R. Jose, C.-C. Yang, MoO_3 Nanoparticle Coatings on High-Voltage 5 V $LiNi_{0.5}Mn_{1.5}O_4$ Cathode Materials for Improving Lithium-Ion Battery Performance, Nanomaterials 12 (2022) 409.

[18] R. Hendriks, D.M. Cunha, D.P. Singh, M. Huijben, Enhanced lithium transport by control of crystal orientation in spinel $LiMn_2O_4$ thin film cathodes, ACS Appl Energy Mater 1 (2018) 7046–7051.

[19] G. Lim, D. Shin, K.H. Chae, M.K. Cho, C. Kim, S.S. Sohn, M. Lee, J. Hong, Regulating dynamic electrochemical interface of $LiNi_{0.5}Mn_{1.5}O_4$ spinel cathode for realizing simultaneous Mn and Ni redox in rechargeable lithium batteries, Adv. Energy Mater. 12 (2022) 2202049.

[20] H. Zhang, F. Li, Z. Li, L. Gao, B. Xu, C. Wang, Surface modification induces oriented Zn (002) deposition for highly stable zinc anode, Batteries 10 (2024) 178.

[21] G. Luo, M. He, L. Zhang, J. Deng, L. Chen, Y. Chao, H. Liu, W. Zhu, Z. Liu, Enhanced lithium extraction from brine using surface-modified $LiMn_2O_4$ electrode with nanoparticle islands, Ind. Chem. Mater. 3 (2025) 353–362.

[22] J. Lu, C. Zhan, T. Wu, J. Wen, Y. Lei, A.J. Kropf, H. Wu, D.J. Miller, J.W. Elam, Y.-K. Sun, Effectively suppressing dissolution of manganese from spinel lithium manganate via a nanoscale surface-doping approach, Nat. Commun. 5 (2014) 5693.

[23] H. Yi, Y. Liang, Y. Qian, Y. Feng, Z. Li, X. Zhang, Low-cost Mn-based cathode materials for lithium-ion batteries, Batteries 9 (2023) 246.

[24] L. Xiao, Y. Guo, D. Qu, B. Deng, H. Liu, D. Tang, Influence of particle sizes and morphologies on the electrochemical performances of spinel $LiMn_2O_4$ cathode materials, J. Power Sources 225 (2013) 286–292.

[25] N. Susarla, S. Ahmed, Estimating cost and energy demand in producing lithium hexafluorophosphate for Li-ion battery electrolyte, Ind. Eng. Chem. Res. 58 (2019) 3754–3766.

[26] G. Kresse, J. Hafner, Ab initio molecular dynamics for liquid metals, Phys. Rev. B 47 (1993) 558.

[27] G. Kresse, J. Hafner, Ab initio molecular-dynamics simulation of the liquid-metal–amorphous-semiconductor transition in germanium, Phys. Rev. B 49 (1994) 14251.

[28] J.P. Perdew, K. Burke, M. Ernzerhof, Generalized gradient approximation made simple, Phys. Rev. Lett. 77 (1996) 3865.

[29] S.L. Dudarev, G.A. Botton, S.Y. Savrasov, C. Humphreys, A.P. Sutton, Electron-energy-loss spectra and the structural stability of nickel oxide: an LSDA+ U study, Phys. Rev. B 57 (1998) 1505.

[30] R. Pulido, N. Naveas, R.J. Martín-Palma, T. Graber, I. Brito, J. Hernández-Montelongo, M.M. Silvan, Experimental and density functional theory study of the Li^+ desorption in spinel/layered lithium manganese oxide nanocomposites using HCl, Chem. Eng. J. 441 (2022) 136019.

[31] N. Ross, S. Willenberg, T. Juqu, E. Carleschi, B.P. Doyle, Boosting $LiMn_2O_4$ Diffusion Coefficients and Stability via Fe/Mg Doping and MWCNT Synergistically Modulating Microstructure, Journal of Nanotechnology 2024 (2024) 7020995.

[32] J. Zhang, H. Guan, J. Yue, Y. Lu, Q. Li, G. Huang, J. Wang, B. Qu, F. Pan, Realization of Mg^{2+} intercalation in a thermodynamically stable layer-structured oxide, RSC Adv. 14 (2024) 32262–32266.

[33] A. Llusco, M. Grageda, S. Ushak, Kinetic and thermodynamic studies on synthesis of Mg-doped $LiMn_2O_4$ nanoparticles, Nanomaterials 10 (2020) 1409.

[34] E. Baris, B. Tanoren, B. Dipcin, F. Guzelcimen, Determination of the significance of atomic concentration on surface properties of $Ba_xMg_{1-x}F_2$ alloy coatings via microscopic and spectroscopic techniques, RSC Adv. 14 (2024) 26043–26049.

[35] A. Haghipour, Electrode engineering of metal-oxide-based materials for optimized lithium-ion batteries, in,, Universität des Saarlandes, 2025.

[36] W.-l. Cheng, Y.-h. Liu, S.-c. Ma, L.-f. Wang, H.-x. Wang, X.-f. Niu, Microstructural characteristics, mechanical and corrosion properties of an extruded low-alloyed Mg-Bi-Al-Zn alloy, Front. Mater. 7 (2020) 55.

[37] H. Tang, C. Cheng, G. Yu, H. Liu, W. Chen, Structure and electrochemical properties of Mg_2SnO_4 nanoparticles synthesized by a facile co-precipitation method, Mater. Chem. Phys. 159 (2015) 167–172.

[38] C.S. Rustomji, Y. Yang, T.K. Kim, J. Mac, Y.J. Kim, E. Caldwell, H. Chung, Y. S. Meng, Liquefied gas electrolytes for electrochemical energy storage devices, Science 356 (2017) eaal4263.

[39] Y.-L. Tong, L. Xing, M.-Z. Dai, X. Wu, Hybrid Co_3O_4@ Co_9S_8 electrocatalysts for oxygen evolution reaction, Frontiers in Materials 6 (2019) 233.

[40] F. Marchini, D. Rubi, M. del Pozo, F.J. Williams, E.J. Calvo, Surface chemistry and lithium-ion exchange in $LiMn_2O_4$ for the electrochemical selective extraction of LiCl from natural salt lake brines, J. Phys. Chem. C 120 (2016) 15875–15883.

[41] H.-h. Li, X.-l. Yang, J.-p. Wei, Z. Zhou, J. Yan, Effect of Mn^{2+} doping on the electrochemical performance of $LiCoPO_4$, J. Electrochem. 14 (2008) 20.

[42] H. Rasheev, A. Seremak, R. Stoyanova, A. Tadjer, Redox hyperactive MOF for Li^+, Na^+ and Mg^{2+} storage, Molecules 27 (2022) 586.

[43] J. Song, Y. Zhang, G. Shao, Comparing the electrochemical performance of $LiFePO_4$/C modified by Mg doping and MgO coating, J. Nanomater. 2013 (2013) 687501.

[44] H. Ouyang, X. Li, Z. Wang, H. Guo, W. Peng, Electrochemical and structural analysis of Mg substitution in lithium-rich layered oxide for lithium-ion battery, Ionics 24 (2018) 3347–3356.

[45] Z. Yang, Y. Wang, X. Chen, H. Wu, Y. Zhang, Mg^{2+} and Ti^{4+} co–doped spinel $LiMn_2O_4$ as lithium-ion battery cathode, ChemistrySelect 4 (2019) 9583–9589.

[46] L. Liu, M. Li, L. Chu, B. Jiang, R. Lin, X. Zhu, G. Cao, Layered ternary metal oxides: Performance degradation mechanisms as cathodes, and design strategies for high-performance batteries, Prog. Mater. Sci. 111 (2020) 100655.

[47] S. Liu, B. Wang, X. Zhang, S. Zhao, Z. Zhang, H. Yu, Reviving the lithium-manganese-based layered oxide cathodes for lithium-ion batteries, Matter 4 (2021) 1511–1527.

[48] K.Y. Chung, W.-S. Yoon, K.-B. Kim, X.-Q. Yang, S.M. Oh, Suppression of structural fatigue by doping in spinel electrode probed by in situ bending beam method, J. Electrochem. Soc. 151 (2004) A484.

[49] Z. Xiao, F. Xia, L. Xu, X. Wang, J. Meng, H. Wang, X. Zhang, L. Geng, J. Wu, L. Mai, Suppressing the Jahn–Teller effect in Mn-based layered oxide cathode toward long-life potassium-ion batteries, Adv. Funct. Mater. 32 (2022) 2108244.

[50] L. Xue, S. Bao, L. Yan, Y. Zhang, J. Lu, Y. Yin, Mgo-coated layered cathode oxide with enhanced stability for sodium-ion batteries, Front. Energy Res. 10 (2022) 847818.

[51] A. Gao, X. Hou, Z. Sun, S. Li, H. Li, J. Zhang, Lithium-desorption mechanism in $LiMn_2O_4$, $Li_{1.33}Mn_{1.67}O_4$, and $Li_{1.6}Mn_{1.6}O_4$ according to precisely controlled acid treatment and density functional theory calculations, J Mater Chem A 7 (2019) 20878–20890.

[52] L. Miao, J. Wu, J. Jiang, P. Liang, First-principles study on the synergistic mechanism of SnO_2 and graphene as a lithium ion battery anode, J. Phys. Chem. C 117 (2013) 23–27.